Boundary Layer Separation on an Airfoil at a Low Reynolds Number

Abdelhafid Bounecer and Lakhdar Bahi

1 Introduction

The advancement in micro-fabrication techniques and miniaturization electronics leads to the development of small unmanned aerial vehicles (UAV), micro aerial vehicles (MAV), and small wind turbines (Sathaye 2004; Yarusevych et al. 2008). Due to their small length scale of about a few centimeters, the MAVs have the ability to fly in urban settings, tunnels, and caves and maintain forward and hovering flight maneuver in such constrained environments (Mahbub et al. 2010; Shyy et al. 2008). The small scale of such technological applications combined to their relatively low speed is the main driving factor for the increasing interest of the low Reynolds number flows over airfoils. Also, this increasing importance is driven by the poor database of the aerodynamic characteristics of the airfoils operating at low Reynolds numbers (10^2–10^5), since most studies on the boundary layer behavior over airfoils have focused on conventional aircraft design with high Reynolds numbers.

The boundary layer separation is the process in which the flow breaks down and detaches from the wall surface. This physical phenomenon can have a large impact on the performance of any vehicle design. When the separation occurs, the boundary layer undergoes a sudden thickening, causing an increased interaction between the viscous and the inviscid layers. Laminar separation occurs when a laminar boundary layer is subject to a sufficiently strong adverse pressure gradient. As the pressure increases along the mean flow direction, the flow velocity decreases. If the pressure differential continues, the flow velocity will eventually come to zero and a

A. Bounecer (✉) • L. Bahi
Mentouri Constantine 1 University, Physics Department, Energy Physics Laboratory,
Ain El Bey, Constantine 25000, Algeria
e-mail: h_bounecer@yahoo.com

reversal of the flow will occur (Neel 1997). The laminar separation zone mainly depends on the pressure gradient, the Reynolds number of the flow, the free-stream turbulence intensity, and the surface roughness. The pressure gradient depends on the airfoil geometry and the angle of attack (Delafin et al. 2014).

Due to the predominance of viscous effects at low Reynolds number, the flow physics is quite complicated, and the boundary layer behaves differently in comparison to its behavior at high Reynolds number. The boundary layer starts to separate at a lower angle of attack as a result of the airfoil curvature changes or the adverse pressure gradient (Shan et al. 2005). A laminar boundary layer starts developing on the suction side of the airfoil. After a certain distance along the airfoil, the flow inside the layer becomes turbulent. At high Reynolds numbers, the transition from laminar to turbulent regime is quick. Thus the turbulent flow inside the layer will be able to effectively overcome the adverse pressure gradient downstream. However, at a low Reynolds number, the boundary layer often remains laminar in the adverse pressure gradient region. When the flow travels far enough against the adverse pressure gradient, the detachment of the boundary layer from the surface of the airfoil will occur. The detached boundary layer may also undergo transition to turbulence, and the resulting turbulent flow may reattach to the airfoil surface. However, when the turbulent mixing momentum is not sufficient, the separated region extends up to the trailing edge (Alam and Sandham 2000; Catalano 2009; Chawla et al. 2009). The location of the separation point, the size of the separated region, and the intensity of the backflow depend on the flow Reynolds number and the angle of attack of the airfoil. These two parameters determine whether the flow reattaches behind the separated zone or remains separated from the airfoil (Hazra and Jamson 2007; Yuan et al. 2007).

At a low Reynolds number, the aerodynamic forces are significantly altered by the boundary layer separation and show a different behavior compared to a high Reynolds number flow (Grager et al. 2011; Günaydinoglu and Kurtulus 2010). Both drag and lift increase with the increasing angle of attack, and at a sufficiently low Reynolds number, the stall is absent over a large range of angles of attack (Kunz 2003; Rajakumar and Ravindran 2010; Zhou et al. 2011).

In the present contribution, a CFD solver based on a finite volume formulation was developed to solve the full Navier-Stokes equations in orthogonal curvilinear form. An orthogonal grid about the airfoil is generated according to the Von Karman-Trefftz conformal mapping. Adam-Bashforth and central difference second-order schemes were used for time and space discretization. The discretized equations are solved according to the SIMPLER algorithm with staggered grid arrangement of the flow variables. The numerical study is conducted for a flow over a NACA0012 airfoil operating at a Reynolds number of 500. After validation tests, velocity profiles, skin friction distribution, and flow pattern, for different angles of attack, are plotted in order to determine the position and the size of the separated region. The aerodynamic coefficients are then evaluated to examine the boundary layer separation effect on the airfoil performance.

Nomenclature

C	Chord length of the airfoil
C_d	Drag coefficient
C_f	Skin friction coefficient
C_1	Lift coefficient
C_p	Pressure coefficient
h_1	Metric parameter in ξ *direction*
h_2	Metric parameter in η *direction*
NACA	*National Advisory Committee for Aeronautics*
Re	Reynolds number based on chord length
U	Horizontal component of physical velocity
$U\xi$	Chordwise computational velocity
$U\eta$	Normal computational velocity
V	Vertical component of physical velocity
x,y	Cartesian coordinates
Greek letters	
α	Angle of attack
τ	Dimensionless time
ξ,η	Curvilinear coordinates

2 Numerical Methods

2.1 Governing Equations

The continuity and momentum equations governing the flow of a fluid can be expressed in an arbitrary time-dependent coordinate system as follows:

$$\frac{\partial \rho}{\partial t} + \vec{\nabla} \bullet \left(\rho \, \vec{V} \right) = 0 \tag{1}$$

$$\frac{\partial}{\partial t} \left(\rho \, \vec{V} \right) + \vec{\nabla} \bullet \rho \, \vec{V} \, \vec{V} = \rho \vec{f} + \vec{\nabla} \bullet \prod_{ij} \tag{2}$$

where ρ is the density, $\vec{V}$ the vector velocity, $\prod$ the stress tensor, and $\vec{f}$ the external forces. The flow is assumed two dimensional, unsteady, incompressible, and viscous. Since the Reynolds number investigated is very low, a fully laminar flow along the airfoil is considered.

The governing equations are transformed into an orthogonal curvilinear coordinate system (ξ,η), such that the coordinates are aligned to the airfoil surface. The nondimensional governing equation form used to solve the problem is based on the free-stream velocity U_∞, the free-stream pressure P_∞, the density ρ, the chord

length C, and the time t. The following orthogonal curvilinear form is given in terms of the nondimensional time τ; the computational velocities $V\xi$, $V\eta$; and the pressure P:

Continuity equation:

$$\frac{1}{h_1 h_2}\frac{\partial}{\partial \varepsilon}\left(\rho\, h_2 V_\varepsilon\right) + \frac{1}{h_1 h_2}\frac{\partial}{\partial \varepsilon}\left(\rho\, h_1 V_\eta\right) = 0 \tag{3}$$

Momentum equation in ξ direction:

$$
\begin{aligned}
\frac{\partial V_\varepsilon}{\partial t} &+ \frac{1}{h_1 h_2}\frac{\partial}{\partial \varepsilon}(h_2 V_\varepsilon V_\varepsilon) + \frac{1}{h_1 h_2}\frac{\partial}{\partial \eta}\left(h_1 V_\varepsilon V_\eta\right) = \\
&-\frac{1}{h_1}\frac{\partial p}{\partial \varepsilon} + \frac{1}{\mathrm{Re}h_2^2}\frac{\partial}{\partial \eta}\left(\frac{V_\varepsilon}{h_1}\right)\frac{\partial h_1}{\partial \eta} - \frac{2}{\mathrm{Re}h_1 h_2^2}\frac{\partial V_\eta}{\partial \eta}\frac{\partial h_2}{\partial \varepsilon} \\
&+\frac{2}{\mathrm{Re}h_1 h_2}\frac{\partial}{\partial \varepsilon}\left(\frac{h_2}{h_1}\frac{\partial V_\varepsilon}{\partial \varepsilon}\right) + \frac{1}{\mathrm{Re}h_1 h_2}\frac{\partial}{\partial \eta}\left(\frac{h_1}{h_2}\frac{\partial V_\varepsilon}{\partial \eta}\right) \\
&+\frac{2}{\mathrm{Re}h_1 h_2}\frac{\partial}{\partial \varepsilon}\left(\frac{V_\eta}{h_1}\frac{\partial h_1}{\partial \eta}\right) + \frac{1}{\mathrm{Re}h_1 h_2}\frac{\partial}{\partial \eta}\left[h_2\frac{\partial}{\partial \varepsilon}\left(\frac{V_\eta}{h_2}\right)\right] \\
&-\frac{1}{\mathrm{Re}h_1 h_2}\frac{\partial}{\partial \eta}\left(\frac{V_\varepsilon}{h_2}\frac{\partial h_1}{\partial \eta}\right) + \frac{1}{\mathrm{Re}h_1^2}\frac{\partial}{\partial \varepsilon}\left(\frac{V_\eta}{h_2}\right)\frac{\partial h_1}{\partial \eta} \\
&-\frac{V_\varepsilon V_\eta}{h_1 h_2}\frac{\partial h_1}{\partial \eta} + \frac{V_\eta^2}{h_1 h_2}\frac{\partial h_2}{\partial \varepsilon} - \frac{2V_\varepsilon}{\mathrm{Re}h_1^2 h_2^2}\left(\frac{\partial h_2}{\partial \varepsilon}\right)^2
\end{aligned}
\tag{4}
$$

Momentum equation in η direction:

$$
\begin{aligned}
\frac{\partial V_\eta}{\partial t} &+ \frac{1}{h_1 h_2}\frac{\partial}{\partial \varepsilon}\left(h_2 V_\varepsilon V_\eta\right) + \frac{1}{h_1 h_2}\frac{\partial}{\partial \eta}\left(h_1 V_\eta V_\eta\right) = \\
&-\frac{1}{h_2}\frac{\partial p}{\partial \eta} + \frac{1}{\mathrm{Re}h_1^2}\frac{\partial}{\partial \varepsilon}\left(\frac{V_\eta}{h_2}\right)\frac{\partial h_2}{\partial \varepsilon} - \frac{2}{\mathrm{Re}h_1^2 h_2}\frac{\partial V_\varepsilon}{\partial \varepsilon}\frac{\partial h_1}{\partial \eta} \\
&+\frac{1}{\mathrm{Re}h_1 h_2}\frac{\partial}{\partial \varepsilon}\left(\frac{h_2}{h_1}\frac{\partial V_\eta}{\partial \varepsilon}\right) + \frac{2}{\mathrm{Re}h_1 h_2}\frac{\partial}{\partial \eta}\left(\frac{h_1}{h_2}\frac{\partial V_\eta}{\partial \eta}\right) \\
&+\frac{1}{\mathrm{Re}h_1 h_2}\frac{\partial}{\partial \varepsilon}\left[h_1\frac{\partial}{\partial \eta}\left(\frac{V_\varepsilon}{h_1}\right)\right] + \frac{2}{\mathrm{Re}h_1 h_2}\frac{\partial}{\partial \eta}\left(\frac{V_\varepsilon}{h_2}\frac{\partial h_2}{\partial \varepsilon}\right) \\
&-\frac{1}{\mathrm{Re}h_1 h_2}\frac{\partial}{\partial \varepsilon}\left(\frac{V_\eta}{h_1}\frac{\partial h_2}{\partial \varepsilon}\right) + \frac{1}{\mathrm{Re}h_2^2}\frac{\partial}{\partial \eta}\left(\frac{V_\varepsilon}{h_1}\right)\left(\frac{\partial h_2}{\partial \varepsilon}\right) \\
&-\frac{V_\varepsilon V_\eta}{h_1 h_2}\frac{\partial h_2}{\partial \varepsilon} + \frac{V_\varepsilon^2}{h_1 h_2}\frac{\partial h_1}{\partial \eta} - \frac{2V_\eta}{\mathrm{Re}h_1^2 h_2^2}\left(\frac{\partial h_1}{\partial \eta}\right)^2
\end{aligned}
\tag{5}
$$

h_1 and h_2 are the metric parameters resulting from the transformation of the equations from the Cartesian coordinate system to the orthogonal curvilinear system. More specific details of the derivation of the Navier-Stokes equations in the curvilinear coordinate system are given by Anderson et al. (1984).

The no-slip and no-penetration boundary conditions are applied on the airfoil surface, and the far-field boundary condition is applied at the outlet of the computational domain, so that the velocity at the boundary is equal to the free-stream velocity.

2.2   Numerical Schemes

The discretization of the governing partial differential equations is based on a finite volume-structured formulation (Patankar 1980; Koshizuka et al. 1990). The major advantage of the finite volume method is that the conservation laws are verified both locally on each finite volume and globally on the whole computational domain. The computational domain is decomposed into quadrilateral elements. The pressure is stored at the nodes, and the two components of the velocity vector are stored at the cell faces in between the nodes. This way, the obtained staggered grid storage of the dependent variables avoids the pressure field oscillations. A second-order accurate Adam-Bashforth scheme is applied for the time integration, and a second-order accurate central difference scheme is applied for the convective term discretization. The SIMPLER algorithm coupled with a staggered storage of the dependent variables is used in order to handle the lake of a proper pressure equation. The resulting algebraic equations system is solved using the cyclic Thomas algorithm (Versteeg and Malalasekera 1995).

2.3   Grid Generation and Time Resolution

Orthogonal conformal grid generation with an O-type topology is obtained by applying the Von Karman-Trefftz transformation (Kitsios et al. 2009). Various grid resolutions are tested to ensure the grid independence of the flow solution. The total number of 33,000 cells is adopted, since the solution exhibits negligible change with farther increase in the number of nodes. The far-field boundary is located at a distance 20 times the chord length, away from the airfoil surface. The grids are clustered near the airfoil surface in the wall-normal direction to resolve the steep gradients within the boundary layer and to capture the physical phenomenon more accurately. A stretching function is used in the transversal coordinate such that the first mesh line will be located at a distance 0.001 time the chord length, from the airfoil surface (Fig. 1).

The time convergence is checked at each time step using the maximum residual velocity components, and a convergence criterion of O (5) is accepted as adequate. A typical time history of the velocity convergence at an arbitrary location within the boundary layer is shown on the Fig. 2.
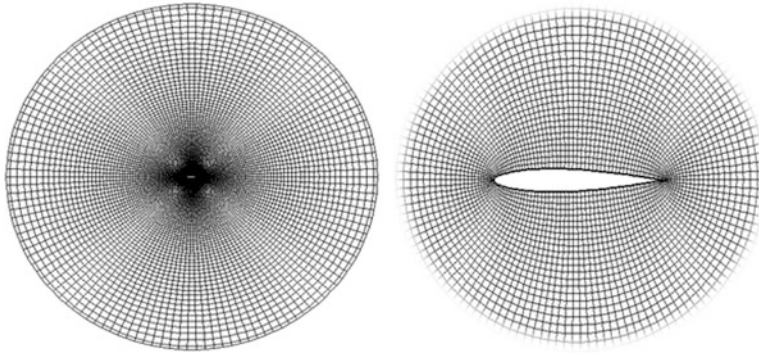
Fig. 1 Structured grid around the airfoil: whole computational domain (*left*) and refined mesh zooming around the airfoil surface (*right*)
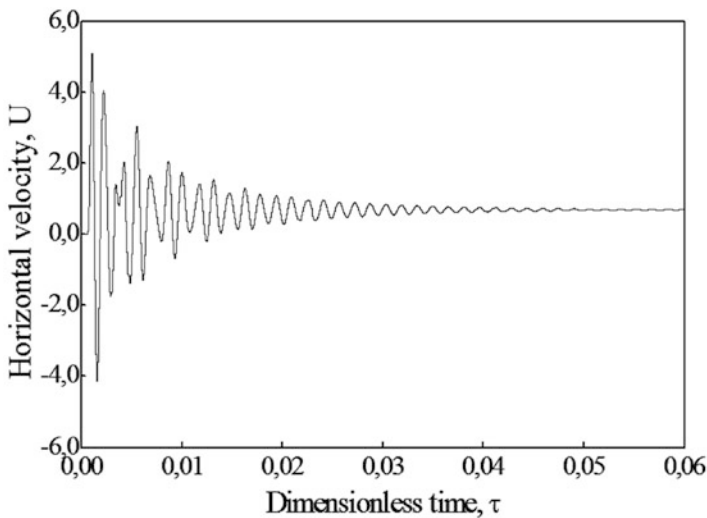

Fig. 2 Velocity history at an arbitrary point within the boundary layer

3   Results and Discussions

The elaborated solver is first validated by applying it to compute the pressure coefficient distribution along a NACA0012 airfoil at a Reynolds number of 500, for two different angles of attack 0° and 10°. The present simulations are compared with those obtained by Hafez et al. (2006), for the same Reynolds number and the angles of attack. Figures 3 and 4 illustrate the good agreement between our results and those of the referenced study. It is worth noting that the maximum discrepancy is less than 5%, despite the different mathematical models used in the two studies. In the present study, the full Navier-Stokes equations are
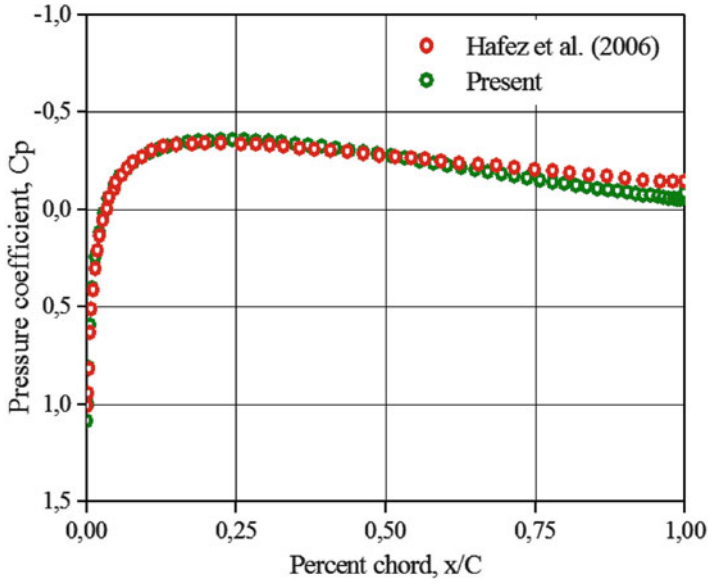
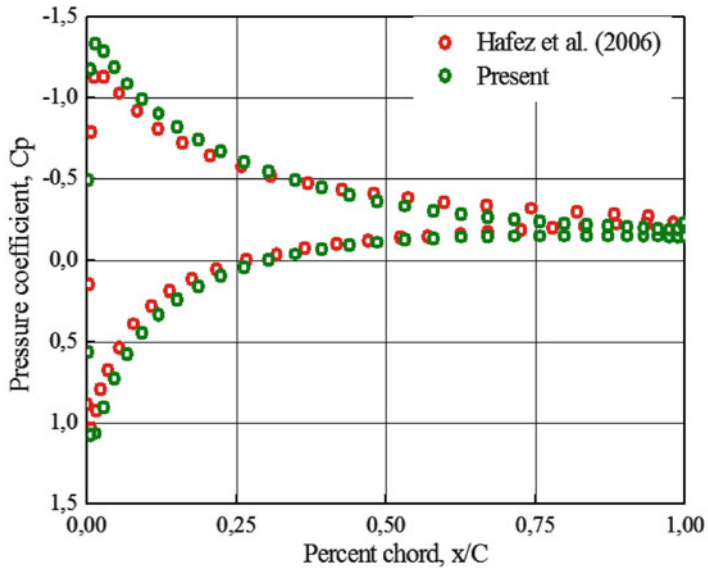**Fig. 3** Pressure coefficient distribution for Re $= 500$, $\alpha = 0°$

Fig. 4 Pressure coefficient distribution for Re $= 500$, $\alpha = 10°$

solved in the whole computational domain, and in the referenced study, the domain is divided to a viscous layer and an external potential layer.

3.1 Boundary Layer Separation

The main attention in the present study is paid to the location of the boundary layer separation, the size, and the strength of the separation bubble.

The separation occurs when the boundary layer encounters an adverse pressure gradient of sufficient magnitude to detach the flow from the airfoil surface. The separation point is defined as the location where the wall shear stress is equal to zero with the apparition of an inflection point on the velocity profile curve. The strength of the separation is defined as the ratio of the maximum reversed flow velocity to the mean flow velocity. The possibility of the reattachment of the separated layer is related to the amount of the momentum transferred to the separated region. If the amount of this momentum is sufficient to cause the necessary pressure rise to overcome the adverse pressure gradient, the reattachment will occur. At a relatively low Reynolds number, the transferred momentum may be insufficient to overcome the adverse pressure gradient and the separated layer may remain detached.

The above parameters of the separation region are studied through the velocity profiles, the skin friction distribution along the airfoil, and the structure of the flow presented by the streamline distribution.

First, velocity profiles as a function of the dimensionless wall-normal coordinates were computed in the boundary layer at three chordwise locations on the suction side of the airfoil: 60%, 80%, and 95%, for 8°, 12°, and 15° of the angle of attack.

In Fig. 5, the angle of attack is set to 8°; the velocity profile curve shows an inflection at 80% chord length from the leading edge, indicating the separation point of the boundary layer. At $x/c = 0.95$, only an accentuated inflection can be seen without revealing the weak strength reversed flow which can be seen later on the flow topology presented by streamline distribution.

Figure 6 shows the velocity profiles at different stations on the suction side of the airfoil for an angle of attack of 12°. The inflection point appears at a station $x/c = 0.60$, followed by a reversed flow beyond this location. The strength of the separation is about 5% at $x/c = 0.80$ station and 10% at $x/c = 0.95$.

At 15° (Fig. 7), the strength of the separation at 60% station is very weak, indicating that the separation point occurs just before this location. The strength of the separation is about 10% at $x/c = 80\%$ and 20% at $x/c = 0.95$. The reversed flow in all stations following the inflection point indicates that the separated boundary layer does not reattach in the remaining part of the upper surface of the airfoil.

The location of the boundary layer separation can be also viewed from the distribution of the skin friction coefficient along the airfoil surface, for different angles of attack. The location of the separation point is defined by a zero skin friction coefficient. Figure 8 shows the skin friction distribution for different angles
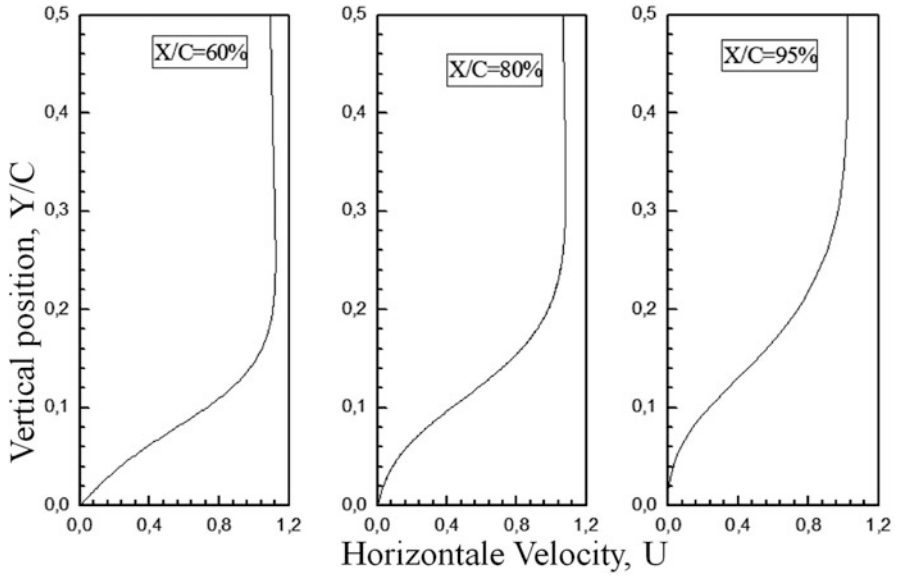
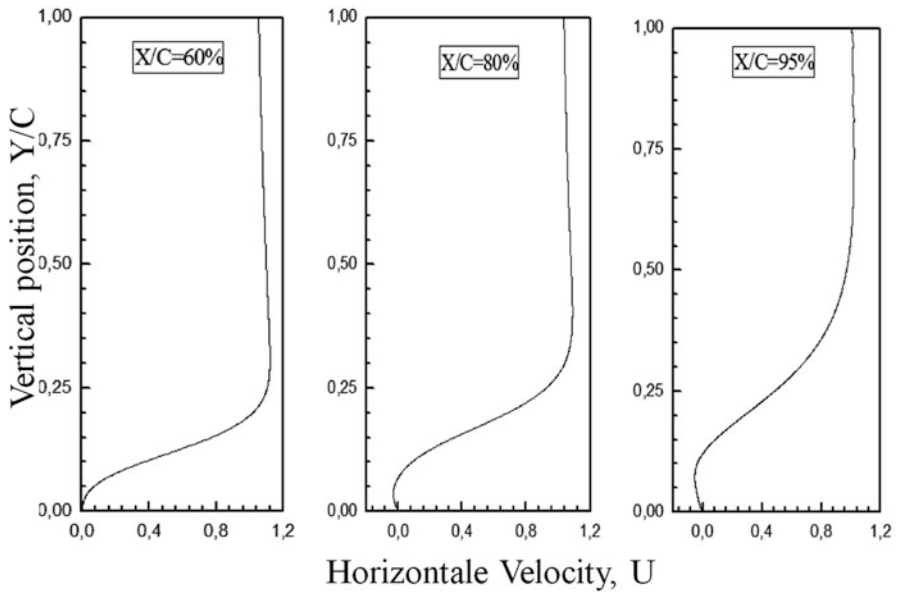Fig. 5 Velocity profiles over a NACA0012 airfoil surface at an angle of attack of 8°, Re = 500

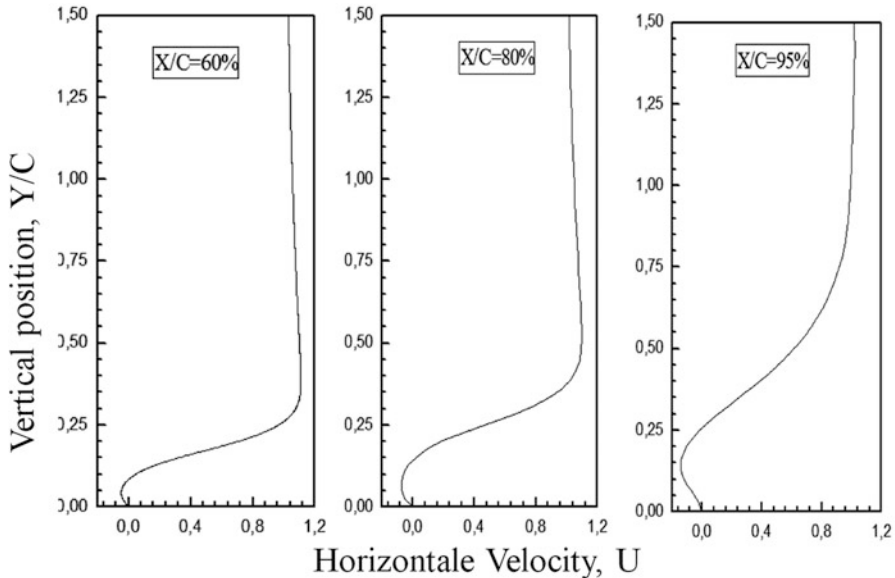Fig. 6 Velocity profiles over a NACA0012 airfoil surface at an angle of attack of 12°, Re = 500

Fig. 7 Velocity profiles over a NACA0012 airfoil surface at an angle of attack of 15°, Re = 500

of attack. It can be seen that between 0° and 5° the skin friction is different from zero, showing that the separation does not occur. However, skin friction on the suction side of the airfoil vanishes from $x/c = 0.8$ at 8° of the angle of attack, $x/c = 0.55$ at 12°, and $x/c = 0.44$ at 15°, indicating that the shear layer is separated and does not reattach.

Streamline distribution at different angles of attack gives a clear view of the minimum onset angle leading to separation, and the evolution of the separated zone as the angle of attack is increasing (Fig. 9). At 8°, a small separation bubble appears near the trailing edge of the airfoil. A further increase in the angle of attack causes an increase in the size of the separation bubble, and the separation point moves toward the leading edge. The location of the separation point for different angles of attack shown on the flow pattern is almost the same location predicted by the velocity profiles and the skin friction distribution.

4 Aerodynamic Performance

In this section, the dependence of the aerodynamic force coefficients on the angle of attack is studied. The mean drag and lift coefficients are computed for each angle of attack using the following relations:
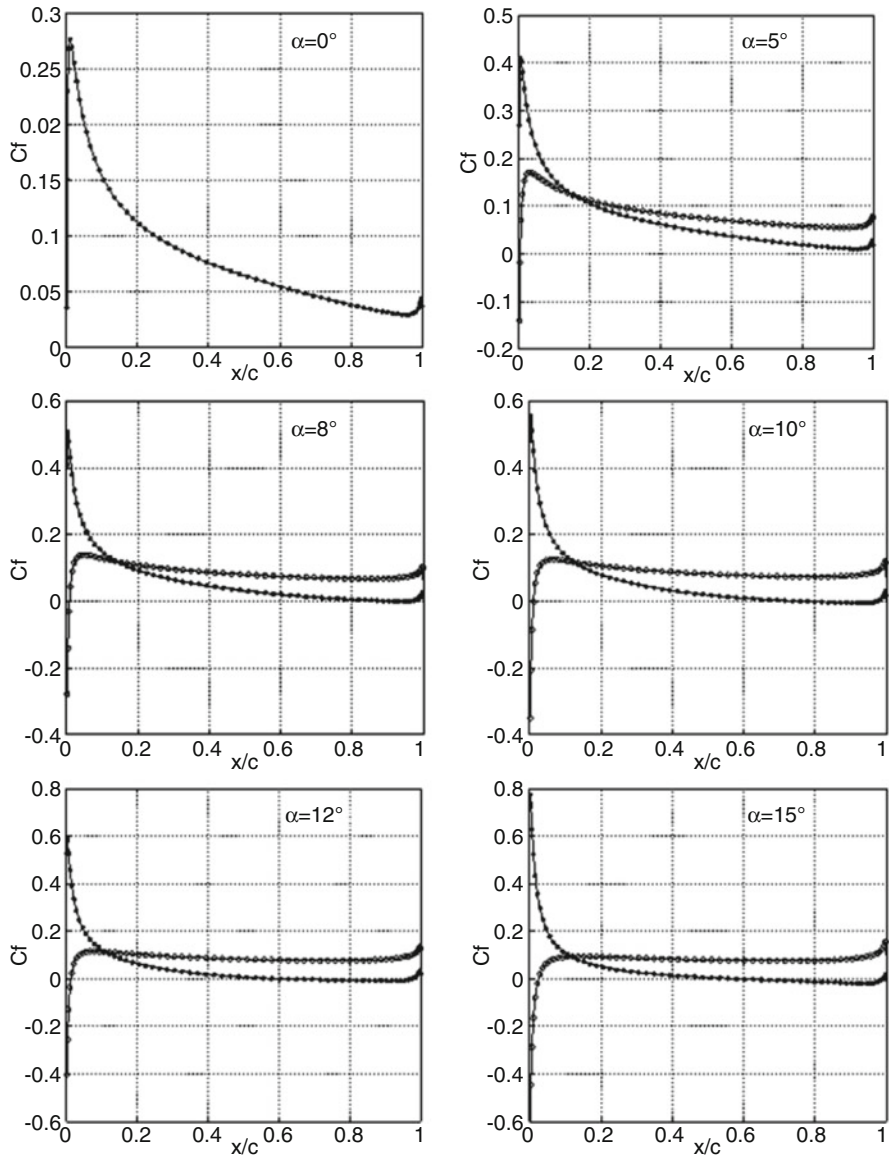
Fig. 8 Skin friction coefficient distribution over a NACA0012 airfoil at Re = 500

$$C_1 = C_n \cos (\alpha) - C_a \sin (\alpha) \tag{6}$$
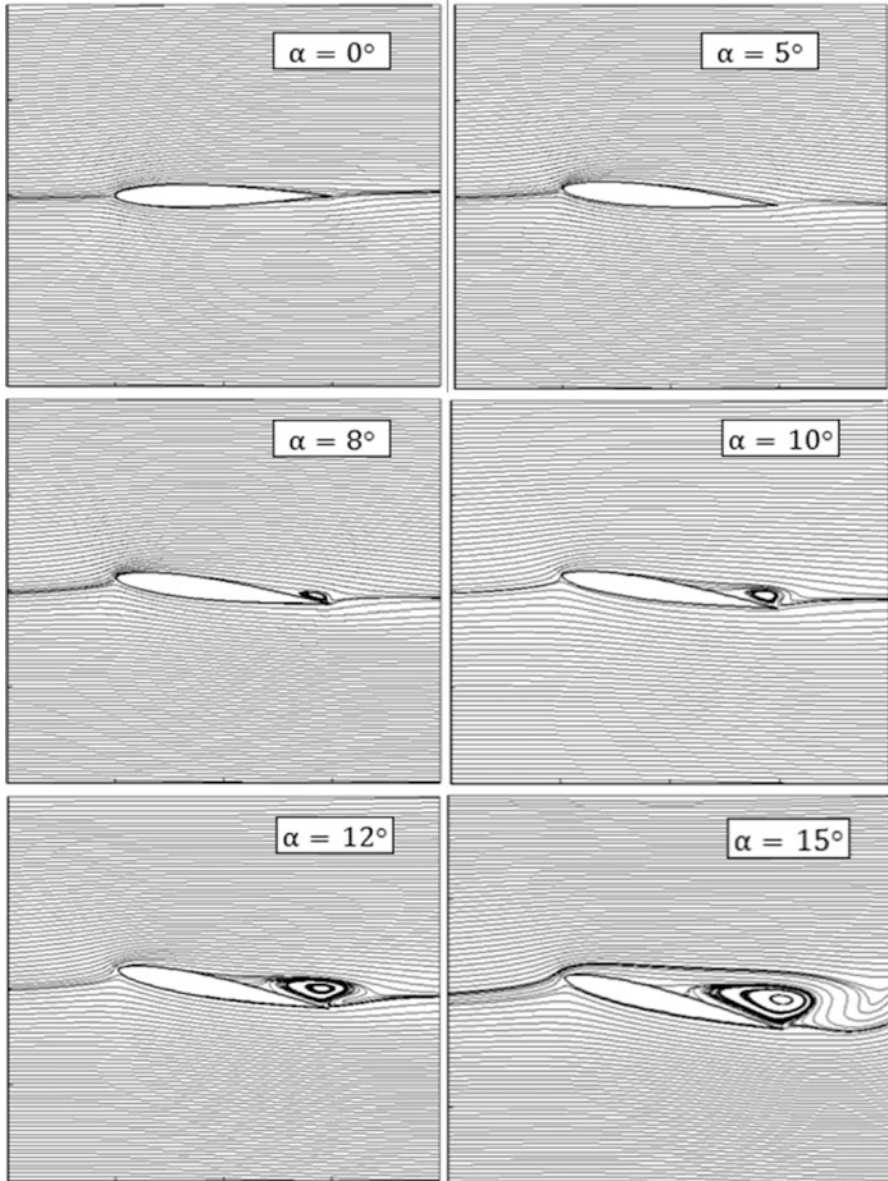
$$C_d = C_n \sin (\alpha) - C_a \cos (\alpha) \tag{7}$$

Fig. 9 Streamline representation about a NACA0012 airfoil at Re = 500

The intermediate coefficients C_n and C_a are obtained by numerical integration of the calculated pressure and skin friction coefficients around the airfoil. More details on the aerodynamic forces calculation are given by Anderson (2007).
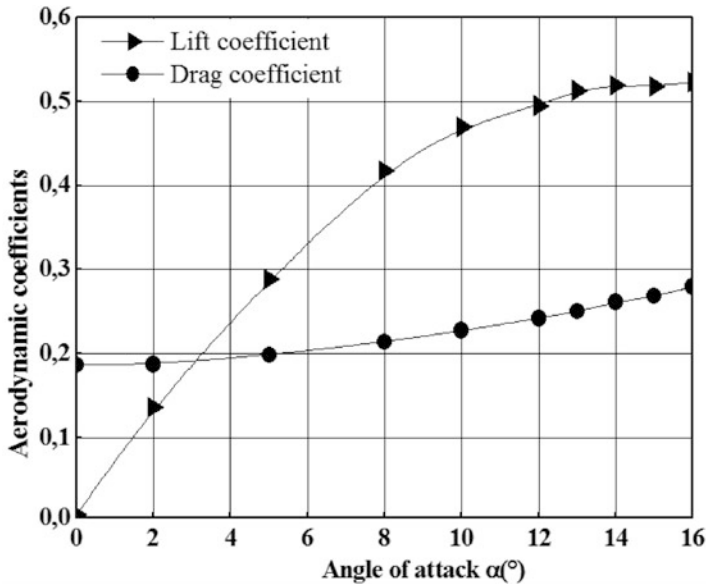
Fig. 10 Lift and drag coefficients variation for NACA0012 profile at Re = 500

The distribution of the lift and drag coefficients over a range of angle of attack is presented in Fig. 10. The lift coefficient keeps increasing with the angle of attack. The increase is almost linear up to $\alpha = 8°$. However, beyond $\alpha = 8°$, the increase slows down indicating the start of the boundary layer separation. A significant decrease in the slope of the lift curve can be seen after the angle 8°. The drop of the lift slope given by $dC_L/d\alpha$, has been estimated to be about 40%.

On the other hand, Fig. 10 shows a moderate increase of the drag coefficient, up to 8°. Beyond this angle of attack, a sudden increase of the drag coefficient takes place. The increase of the drag coefficient slope expressed by $dC_d/d\alpha$ has been estimated to be about 58%.

The lift-drag polar (Fig. 11) illustrates the dependence of the lift coefficient on the drag coefficient with the angle of attack. Up to the angle of separation 8° where the boundary layer is attached, the lift and drag exhibit a strong dependence. Beyond the angle 8°, the separation of the boundary layer causes a significant reduction in the dependence of the two aerodynamic coefficients. The ratio CL/CD indicated by the curve tangent increases rapidly before separation and slows down suddenly just beyond the onset separation angle.
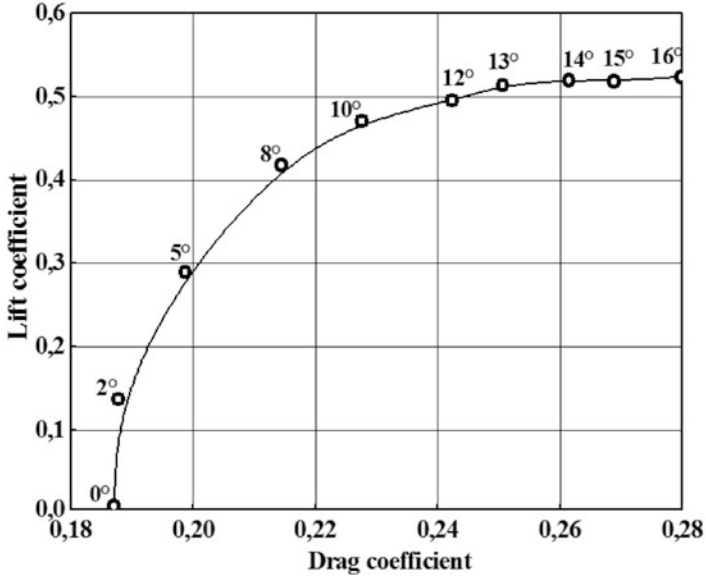
Fig. 11 Polar of NACA0012 airfoil at Re = 500

5 Conclusions

A numerical simulation has been carried out to study the separation of the boundary layer on a NACA0012 airfoil for a Reynolds number of 500. The computations were performed for a range of angles of attack. The finite volume method is used to discretize the incompressible full Navier-Stokes equations, written in curvilinear coordinates. For this purpose a computer solver implementing the numerical algorithm is developed. To handle the complexity of the airfoil geometry, a procedure for orthogonal grid generation based on conformal mapping is combined to the solver. The accuracy of the developed solver has been tested in computing the pressure coefficient distribution along a NACA0012 airfoil. The computed pressure compared favorably with the previous available data of Hafez et al. (2006). Indeed, the solver allows us to predict the boundary layer separation though the velocity profiles, the skin friction distribution, and the flow structure. It had been found that the separation zone begins to appear at 8° of the angle of attack. The separated zone grows and advances toward the leading edge of the airfoil with the increase of the angle of attack.

The flow separation affects substantially the aerodynamic performance. The amount of the increase of the lift coefficient is reduced by about 40%, and the drag coefficient increasing is raised by about 58%, just beyond the angle of attack at which the separation begins.

References

Alam, M., Sandham, N.D.: Direct numerical simulation of short laminar separation bubbles with turbulent reattachment. J. Fluid Mech. **410**, 1–28 (2000)

Anderson, J.D.: Fundamentals of Aerodynamics, 3rd edn. McGraw-Hill, New York (2007)

Anderson, A., Tannehill, C., Pletcher, H.: Computational Fluid Mechanics and Heat Transfer. Hemisphere Publishing Corporation, New York (1984)

Catalano, P.: Aerodynamic Analysis of Low Reynolds Number Flows, Ph.D. Thesis, Aerospatiale Engineering, Napoli University (2009)

Chawla, J.S., Suryanarayanan, S., Falzon, B.: Low Reynolds number flow over airfoils, Seminar report, Mechanical Engineering, Indian institute of technology, Bombay (2009)

Delafin, P.L., Deniset, F., Asotolfi, J.A.: Effect of the laminar separation bubble induced transition on the hydrodynamic performance of a hydrofoil. Eur. J. Mech. B/Fluids. **46**, 190–200 (2014)

Grager, T., Rothmayer, A., Hu, H.: Stall suppression of a low-Reynolds-number airfoil with a dynamic burst control plate, 49th AIAA Aerospace science meeting including the new horizons forum and aerospace exposition, Orlando, Florida (2011)

Günaydinoglu, E., Kurtulus, D.F.: Effect of vertical translation on unsteady aerodynamics of hovering airfoil, Fifth European Conference on Computational Fluid Dynamics ECCOMAS CFD, Lisbon, Portugal (2010)

Hafez, M., Shatalov, A., Wahba, E.: Numerical simulations of incompressible aerodynamic flows using viscous/inviscid interaction procedures. Comput. Methods Appl. Mech. Eng. **195**, 3110–3127 (2006)

Hazra, S.B., Jamson, A.: Aerodynamic Shape Optimization of Airfoils in Ultra-low Reynolds Number Flow Using Simultaneous Pseudo-Time Stepping, Aerospace Computing Lab (ACL) Report 2007–4. Stanford University, USA (2007)

Kitsios, V., Rodriguez, D., Theofilis, V., Ooi, A., Soria, J.: BiGlobal stability analysis in curvilinear coordinates of massively separated lifting bodies. J. Comput. Phys. **228**, 7181–7196 (2009)

Koshizuka, S., Oka, Y., Kondo, S.: A staggered differencing technique on boundary curvilinear grids for incompressible flows along curvilinear or slant walls. J. Comput. Mech. **7**, 123–136 (1990)

Kunz, P.: Aerodynamics and Design for Ultra-Low Reynolds Number Flight, Ph.D. Thesis, Stanford university (2003)

Mahbub, M.D., Zhou, Y., Yang, H.V.: The ultra-low Reynolds number airfoil wake. Exp. Fluids. **48**, 81–103 (2010)

Neel, R.E.: Advances in Computational Fluid Dynamic Turbulent Separated Flows and Transonic Potential Flows, Ph.D. Thesis, Mechanical Department, Univ. of state (1997)

Patankar, V.: Numerical Heat Transfer and Fluid Flow. Hemisphere Publishing Corporation, New York, USA (1980)

Rajakumar, S., Ravindran, D.: Computational fluid dynamics of wind turbine blade at various angles of attack and low Reynolds number. Int. J. Eng. Sci. Technol. **2**(11), 6474–6484 (2010)

Sathaye, S.S.: Lift Distribution on Low Aspect Ratio Wings at Low Reynolds Numbers, Master's Thesis, Worcester Polytechnic Institute (2004)

Shan, H., Jiang, L., Liu, C.: Direct numerical simulation of flow separation around a NACA0012 airfoil. Comput. Fluids. **34**, 1096–1114 (2005)

Shyy, W., et al.: Computational Aerodynamics of low Reynolds number Plunging, Pitching and Flexible Wings for MAV Applications, 46th AIAA Aerospace science meeting and exhibit, 7–10 January 2008, Reo, NEVADA (2008)

Versteeg, K., Malalasekera, W.: An Introduction to Computational Fluid Dynamics: the Finite Volume Method. Longman Group Ltd, Harlow, England (1995)

Yarusevych, S., Kawall, J.G., Sullivan, P.E.: Separated-Shear-Layer development on an airfoil at low Reynolds numbers. AIAA J. **46**(12), 3060–3069 (2008)

Yuan, W., Khalid, M., Windte, J., Scholz, U., Radespiel, R.: Computational and experimental investigations of low-Reynolds-number flows past an airfoil. Aeronaut. J. **111**(1115), 17–29 (2007)

Zhou, Y., Alam, M., Yang, X., Guo, H., Wood, H.: Fluid forces on a very low Reynolds number airfoil and their prediction. Int. J. Heat Fluid Flow. **32**, 329–339 (2011)